The Astrophysical Journal, 834:143 (16pp), 2017 January 10 https://doi.org/10.3847/1538-4357/834/2/143

THE GOULD'S BELT DISTANCES SURVEY (GOBELINS). III. THE DISTANCE TO THE SERPENS/AQUILA MOLECULAR COMPLEX

Gisela N. Ortiz-León[1], Sergio A. Dzib[2], Marina A. Kounkel[3], Laurent Loinard[1,2], Amy J. Mioduszewski[4], Luis F. Rodríguez[1], Rosa M. Torres[5], Gerardo Pech[1], Juana L. Rivera[1], Lee Hartmann[3], Andrew F. Boden[6], Neal J. Evans II[7], Cesar Briceño[8], John J. Tobin[9,10], and Phillip A. B. Galli[11,12]
[1] Instituto de Radioastronomía y Astrofísica, Universidad Nacional Autónoma de México, Morelia 58089, México; g.ortiz@crya.unam.mx
[2] Max Planck Institut für Radioastronomie, Auf dem Hügel 69, D-53121 Bonn, Germany
[3] Department of Astronomy, University of Michigan, 500 Church Street, Ann Arbor, MI 48105, USA
[4] National Radio Astronomy Observatory, Domenici Science Operations Center, 1003 Lopezville Road, Socorro, NM 87801, USA
[5] Centro Universitario de Tonalá, Universidad de Guadalajara, Avenida Nuevo Periférico No. 555, Ejido San José Tatepozco, C.P. 48525, Tonalá, Jalisco, México
[6] Division of Physics, Math and Astronomy, California Institute of Technology, 1200 East California Boulevard, Pasadena, CA 91125, USA
[7] Department of Astronomy, The University of Texas at Austin, 2515 Speedway, Stop C1400, Austin, TX 78712-1205, USA
[8] Cerro Tololo Interamerican Observatory, Casilla 603, La Serena, Chile
[9] Homer L. Dodge Department of Physics and Astronomy, University of Oklahoma, 440 W. Brooks Street, Norman, OK 73019, USA
[10] Leiden Observatory, P.O. Box 9513, NL-2300 RA, Leiden, The Netherlands
[11] Instituto de Astronomia, Geofísica e Ciências Atmosféricas, Universidade de São Paulo, Rua do Matão 1226, Cidade Universitária, São Paulo, Brazil
[12] Univ. Grenoble Alpes, IPAG, F-38000, Grenoble, France
Received 2016 September 6; revised 2016 October 10; accepted 2016 October 10; published 2017 January 11

ABSTRACT

We report on new distances and proper motions to seven stars across the Serpens/Aquila complex. The observations were obtained as part of the Gould's Belt Distances Survey (GOBELINS) project between 2013 September and 2016 April with the Very Long Baseline Array (VLBA). One of our targets is the proto-Herbig AeBe object EC 95, which is a binary system embedded in the Serpens Core. For this system, we combined the GOBELINS observations with previous VLBA data to cover a total period of 8 years, and derive the orbital elements and an updated source distance. The individual distances to sources in the complex are fully consistent with each other, and the mean value corresponds to a distance of 436.0 ± 9.2 pc for the Serpens/W40 complex. Given this new evidence, we argue that Serpens Main, W40, and Serpens South are physically associated and form a single cloud structure.

Key words: astrometry – radiation mechanisms: non-thermal – radio continuum: stars – techniques: interferometric

1. INTRODUCTION

The Serpens molecular cloud is a region rich in low-mass star formation selected for observations as part of the Gould's Belt Distances Survey (GOBELINS; Ortiz-León et al. 2017). There are two smaller regions, of $\sim$1 deg^2 in size, associated with this cloud: Serpens Main and Serpens South. Serpens Main (centered on R.A. $18^h29^m00^s$, decl. $+00^o30'00''$; Eiroa et al. 2008) consists of three prominent subregions, namely, the Serpens core, Serpens G3-G6, and VV Serpentis. Its northernmost subregion is the Serpens core (also called Serpens North or Cluster A; Harvey et al. 2006), a cluster of YSOs deeply embedded with extinction exceeding 40 mag in the visual. This subregion has numerous observations from X-rays to the submillimeter that have revealed a large population of protostars (e.g., Kaas et al. 2004; Eiroa et al. 2005; Harvey et al. 2006, 2007; Winston et al. 2007, 2009; Oliveira et al. 2010). Serpens G3-G6 (Cohen & Kuhi 1979), also referred to as Cluster B, was identified by Harvey et al. (2006) as a cluster of star formation harboring many previously unknown young stellar objects (YSOs). Finally, VV Serpentis is the southernmost subregion associated with the eponymous star. Currently, the most extensive study of the young stellar population in Serpens Main was conducted by the *Spitzer* Legacy Program "From Molecular Cores to Planet-Forming Disks" (c2d; Evans et al. 2003), where more than 200 Class 0 to Class III YSOs associated with IR excess were identified in an area of 0.85 deg^2 (Dunham et al. 2015). Serpens South (centered on R.A. $18^h30^m00^s$, decl. $-02^o02'00''$, i.e., at an angular distance of $\sim3^o$ south of Serpens Main) was discovered by Gutermuth et al. (2008). Since then, it has received a lot of attention because of the large number of extremely young objects that it contains. It shows an unusually large fraction of protostars (Gutermuth et al. 2008), presenting an excellent laboratory to study the earliest stages of star formation.

To the east of Serpens South, at R.A. $\sim 18^h31^m29^s$, decl. $-02^o05'24''$, lies the W40 complex, named after the H II region also known as Sharpless 2–64 (Smith et al. 1985; Vallee 1987). This complex shows evidence for ongoing star formation since it contains dense molecular cores (Dobashi et al. 2005), millimeter-wave sources (Molinari et al. 1996; Maury et al. 2011), and YSOs (Kuhn et al. 2010; Rodríguez et al. 2010; Mallick et al. 2013). There is also a cluster of massive stars that ionizes the H II region (Smith et al. 1985; Shuping et al. 2012). Both Serpens South and W40 belong to a larger complex of molecular clouds collectively known as the *Aquila Rift*, a large elongated feature seen in 2MASS extinction maps (Bontemps et al. 2010). The Aquila Rift was one of the clouds targeted by the *Herschel* (André et al. 2010; Könyves et al. 2015) and *Spitzer* (Dunham et al. 2015) Gould Belt Surveys, which revealed hundreds of YSOs all across the complex. Figure 1 shows the location of the Serpens Main region as well as the position of W40 and Serpens South within the Aquila Complex. We note that although Serpens and the Aquila Rift do not formally belong to the Gould's Belt, they are usually included in Gould Belt Surveys because of their star formation activity and because they were previously thought to be closer to the Sun.

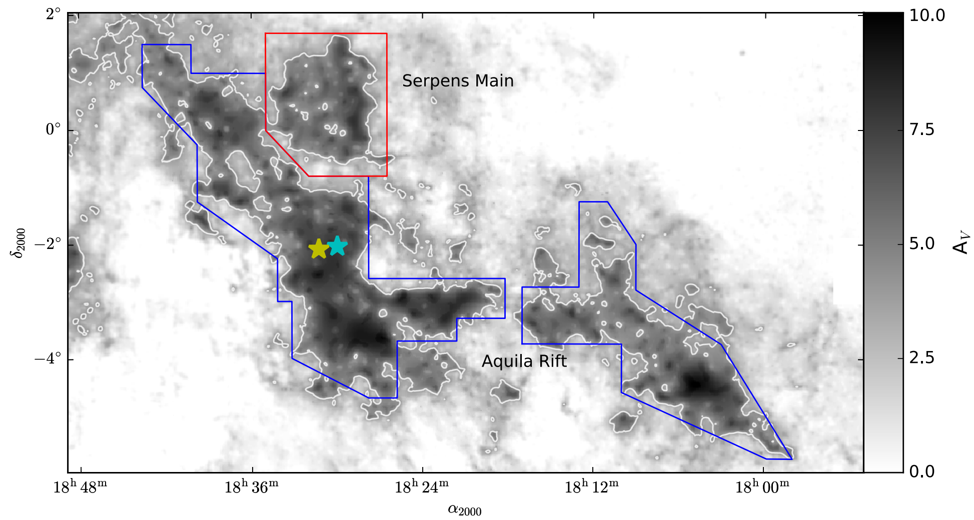

Figure 1. Extinction map of the Serpens and Aquila star-forming regions obtained as part of the COMPLETE project, based on the STScI Digitized Sky Survey data (Cambrésy 1999). Red and blue polygons mark the structures corresponding to Serpens Main and the Aquila Rift, respectively, while cyan and yellow stars indicate the center of the W40 and Serpens South regions. The white contour indicates an A_V of 4.

The distances to the different regions in the Serpens/Aquila Complex have been a matter of controversy. For Serpens Main, there is an ample range of distances reported in the literature, from 245 ± 30 pc (Chavarria-K et al. 1988) to 650 ± 180 pc (Zhang et al. 1988). Most of these estimates are indirect, since they are often based on spectroscopic parallaxes and extinction measurements. Winston et al. (2010) constructed the X-ray luminosity function of the Serpens cluster using different distances to calculate the X-ray luminosity and fitted the data with the distribution determined by Feigelson & Getman (2005) for Orion, IC 348, and NGC 1333. The best fit to the data was found to be at a distance to Serpens of 360^{+22}_{-13} pc. The only direct measurement of the distance to Serpens Main has been obtained by Dzib et al. (2010, 2011) from the Very Long Baseline Interferometry (VLBI) trigonometric parallax of the YSO EC 95 associated with the Serpens Core. These authors derived a distance to the Serpens Core of 415 ± 5 pc and a mean distance to the Serpens cloud of 415 ± 25 pc. Later, they updated the distance to the Core to 429 ± 2 pc. However, the usually adopted distance for Serpens Main and the Aquila Rift as well is 259 ± 37 pc, which was derived by Straižys et al. (1996) from photometry of ∼100 optically visible stars, 18 of which belong to Serpens Main. In a more recent paper, Straižys et al. (2003) used 80 stars from their original sample, as well as 400 other stars, to measure the distance to the front edge of the dark clouds (the extinction wall) in the Serpens/Aquila complex. They placed this wall at 225 ± 55 pc, and suggested that the cloud is about 80 pc deep.

As we mentioned earlier, W40 and Serpens South are embedded within the Aquila Rift. Estimates of the distance to W40 seem to favor values between 455 and 600 pc (Kolesnik & Iurevich 1983; Shuping et al. 2012), which suggests this cloud lies somewhat farther away than the extinction wall of the Aquila Rift. So far, there are no distance measurements to sources in Serpens South, but many authors argue that the region is at the same distance as Serpens Main, and adopt either 260 or 429 pc (e.g., Gutermuth et al. 2008; Maury et al. 2011; Heiderman & Evans 2015; Plunkett et al. 2015; Kern et al. 2016). It has also been argued that W40 and Serpens South belong to the same continuous extinction feature and should be part of the same complex, likely at the same distance (Maury et al. 2011).

In this paper, we report on the distance to three stars in the Serpens cloud core and four objects in the W40 cluster. The observations were obtained as part of the GOBELINS project (Ortiz-León et al. 2017) with the Very Long Baseline Array (VLBA). We describe our targets and observations in Section 2. The astrometry of our sources is given in Section 3. Finally, we discuss our findings in Section 4 and provide a summary in Section 5.

2. TARGET SELECTION AND OBSERVATIONS

While both thermal and non-thermal processes produce radio emission in young stars, only brightness temperatures $\gtrsim 10^6$ K will be detectable on VLBI baselines (Thompson et al. 2007), which limits VLBI observations to non-thermal radiation. Thus, our targets consist of young stars with potentially non-thermal radio emission. This kind of emission is expected to be produced in the coronae of magnetically active stars by energetic electrons gyrating around the magnetic field lines (Feigelson & Montmerle 1999).

In Ortiz-León et al. (2015), we reported on deep radio observations carried out with the Karl Jansky Very Large Array (VLA) of three of the most prominent regions in the Serpens/Aquila Complex, namely, the Serpens Core, W40, and Serpens South. A total of 18 possible targets (known or candidate YSOs) for VLBA astrometry were identified across these three regions, based on their compactness, negative spectral index, and/or variability. The VLBA was pointed at the positions of the 18 candidates; however, we also correlated (i.e., changed the phase center of the correlation) at the positions of the other sources that lie in the primary beam of the individual VLBA telescopes (of 10′ in size at 5 GHz). This provided an additional 63 sources, 3 of which turned out to be YSOs with detectable non-thermal radio emission.

We refer the reader to Ortiz-León et al. (2017) for a detailed description of our observing approach. Briefly, the VLBA observations of GOBELINS were taken between 2013 September and 2016 April at $\nu = 4.9$ or 8.3 GHz (C- and

Table 1
Observed Epochs

Project Code	Observation Date	VLBA Pointing Positions R.A. (α_{2000})	Decl. (δ_{2000})	Observed Band
BL175E0	2013 Sep 01	18:29:10.178	+01:25:59.56	C
		18:29:27.366	+01:20:37.43	
BL175E1	2013 Sep 02	18:29:30.714	+01:00:48.31	C
		18:29:47.838	+01:14:21.66	
BL175E2	2013 Sep 03	18:30:44.115	−02:01:45.66	C
		18:31:21.969	−02:04:52.54	
BL175E3	2013 Sep 05	18:29:49.507	+01:19:55.88	C
		18:29:52.736	−01:51:59.93	
BL175E4	2013 Sep 07	18:31:21.141	−02:04:31.08	X
		18:29:16.120	+01:04:37.58	
		18:29:33.073	+01:17:16.39	
BL175DX	2014 Feb 17	18:31:18.685	−01:54:55.99	X
BL175G0	2014 Mar 01	18:29:10.178	+01:25:59.56	C
		18:29:27.366	+01:20:37.43	
BL175G1	2014 Mar 03	18:29:30.714	+01:00:48.31	C
		18:29:47.838	+01:14:21.66	
BL175G2	2014 Mar 04	18:31:21.969	−02:04:52.54	C
		18:30:44.115	−02:01:45.66	
BL175G3	2014 Mar 06	18:29:49.507	+01:19:55.88	C
		18:29:52.736	−01:51:59.93	
BL175G4	2014 Mar 09	18:29:16.120	+01:04:37.58	X
		18:29:33.073	+01:17:16.39	
BL175GC	2014 Apr 01	18:28:54.46	+01:18:23.78	C
		18:29:48.83	+01:06:47.46	
BL175CR	2014 Oct 07	18:29:10.178	+01:25:59.56	C
		18:29:27.366	+01:20:37.43	
BL175CS	2014 Oct 12	18:29:30.714	+01:00:48.31	C
		18:29:47.838	+01:14:21.66	
BL175CT	2014 Oct 15	18:31:21.969	−02:04:52.54	C
		18:30:44.115	−02:01:45.66	
BL175EX	2015 Feb 27	18:29:10.178	+01:25:59.56	C
		18:29:27.366	+01:20:37.43	
BL175EY	2015 Mar 02	18:29:47.838	+01:14:21.66	C
		18:31:18.685	−01:54:55.99	
BL175EZ	2015 Mar 20	18:31:21.969	−02:04:52.54	C
		18:30:44.115	−02:01:45.66	
BL175GT	2015 Sep 15	18:28:54.46	+01:18:23.78	X
		18:29:48.83	+01:06:47.46	
BL175GU	2015 Sep 19	18:31:21.969	−02:04:52.54	C
		18:30:44.115	−02:01:45.66	
BL175GW	2015 Oct 04	18:29:10.178	+01:25:59.56	C
		18:29:27.366	+01:20:37.43	
BL175GX	2015 Oct 06	18:29:47.838	+01:14:21.66	C
		18:31:18.685	−01:54:55.99	
BL175GV	2015 Oct 11	18:31:21.141	−02:04:31.08	C
		18:29:16.120	+01:04:37.58	
		18:29:33.073	+01:17:16.39	
BL175GY	2015 Oct 13	18:29:49.507	+01:19:55.88	C
		18:29:52.736	−01:51:59.93	
BL175CU	2016 Feb 29	18:29:52.736	−01:51:59.93	C
		18:31:21.141	−02:04:31.08	
BL175F4	2016 Mar 20	18:29:33.073	+01:17:16.39	X
BL175F8	2016 Apr 28	18:29:47.838	+01:14:21.66	C

X-bands, respectively). The data were recorded in dual polarization mode with 256 MHz of bandwidth in each polarization, covered by eight separate 32 MHz intermediate frequency (IF) channels. VLBA project codes, observing dates, pointing positions, and corresponding observing bands are given in Table 1. Several sets of phase calibrators were chosen according to their angular separations relative to target positions and used for multi-source phase referencing. The corresponding sets of calibrators for each pointing position (target) are listed in Table 2. One or two targets were observed in each observing session. These consisted of cycles alternating between the target(s) and the main phase calibrator: target–calibrator for single-target sessions, and target 1–calibrator–target 2–calibrator for those sessions where two targets were observed simultaneously. The secondary calibrators were observed every ∼50 minutes. The total integration time for each target was ∼1.6 hr in projects that observed at 8.3 GHz, and ∼1 hr at 4.9 GHz. Geodetic-like blocks, consisting of observations of many calibrators over a wide range of elevations, were taken before and after each session. These were observed with 512 MHz total bandwidth covered by 16 IFs and centered at $\nu = 4.6$ and 8.1 GHz for projects observing at the C- and X-bands, respectively.

Table 2
Setup of Calibrators

R.A. (J2000)	Decl. (J2000)	Calibrators[a]
18:29:52.736	−01:51:59.93	J1834–0301, J1833+0115, J1824+0119, J1821–0502
18:31:21.141	−02:04:31.08	
18:29:47.838	+01:14:21.66	J1833+0115, J1826+0149, J1824+0119, J1832+0118
18:29:30.714	+01:00:48.31	
18:28:54.460	+01:18:23.78	J1832+0118, J1833+0115, J1826+0149, J1824+0119
18:29:48.830	+01:06:47.46	
18:31:21.969	−02:04:52.54	J1834–0301, J1833+0115, J1824+0119, J1821–0502
18:30:44.115	−02:01:45.66	
18:29:16.120	+01:04:37.58	J1826+0149, J1833+0115, J1824+0119, J1832+0118
18:29:33.073	+01:17:16.39	
18:29:10.178	+01:25:59.56	
18:29:27.366	+01:20:37.43	
18:29:33.073	+01:17:16.39	
18:31:18.685	−01:54:55.99	J1834–0301, J1824+0119, J1819–0258, J1833+0115
18:29:49.507	+01:19:55.88	J1826+0149, J1832+0118, J1833+0115, J1824+0119

Note.
[a] First source in the list corresponds to main phase calibrator.

Data reduction was performed using AIPS (Greisen 2003), following the strategy described in Ortiz-León et al. (2017). Calibrated visibilities were imaged using a pixel size of 50–100 μas and pure natural weighting. Typical angular resolutions were 4 mas × 2 mas (∼1.3 au at a distance of 429 pc) at 4.9 GHz and 3 mas × 0.9 mas (∼0.8 au) at 8.3 GHz. Noise levels were typically 30 and 38 μJy beam^{-1} at the C- and X-bands, respectively.

In addition, we will use data from VLBA projects BL155 and BL160 (P.I.: L. Loinard) and BD155 (P.I.: S. Dzib), which

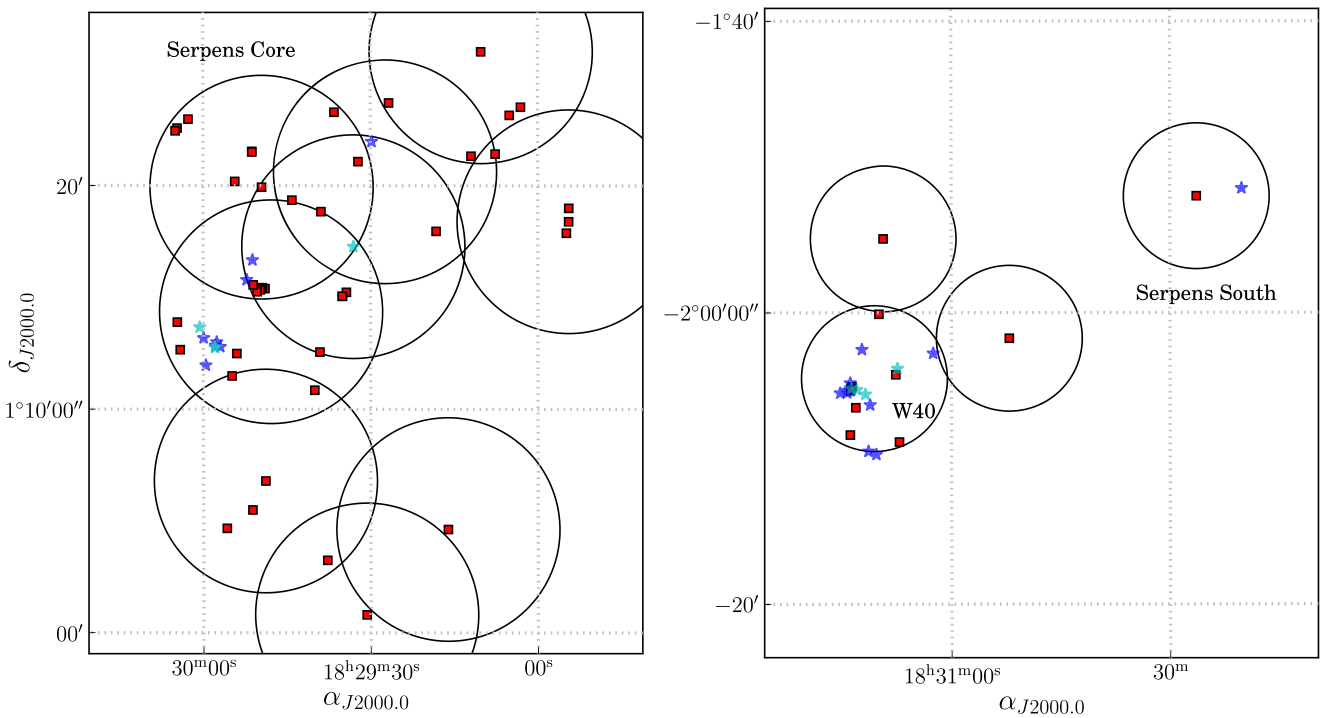

Figure 2. Spatial distribution of observed sources in the Serpens Core (left) and W40/Serpens South (right). Blue and cyan stars correspond to known YSOs and YSOs with a distance estimation provided in this paper, respectively. Red squares mark the positions of other unclassified observed sources.

were designed to only observe the source EC 95 between 2007 December and 2016 January at $\nu = 8.4$ GHz. The images corresponding to these old observations have noise levels of 76 μJy beam^{-1}.

3. RESULTS

As mentioned earlier, we observed a total of 81 sources in the Serpens/Aquila region. Their spatial distribution is shown in Figure 2, while the source VLA coordinates, names, types, fluxes, and brightness temperatures, T_b, are given in the first eight columns in Table 3. Out of the total observed sources, 30 have been firmly detected. These are sources detected in several epochs, with at least one detection at 5σ, or sources detected just in one epoch but at 6σ, where σ is the rms noise measured in the images. All sources show $T_b > 10^6$ K, consistent with the brightness temperature expected for non-thermal emission.

3.1. Individual Distances: Single Stars

Source positions at individual epochs were extracted by performing two-dimensional Gaussian fits with the AIPS task JMFIT. These and the associated uncertainties provided by JMFIT, which are based on the expected theoretical astrometric precision of an interferometer (Condon 1997), are listed in Table 7. We analyze the motion of all objects detected in at least two epochs. A total of 20 objects, which do not have a firm classification in the literature, show a motion consistent with that expected for background sources, i.e., their positions remain systematically unchanged within the positional errors, or even if they move, their derived parallaxes correspond to distances larger than 1 kpc. This can be seen grapically in Figure 3. The horizontal axis of this plot corresponds to the *position change rate* in milli-arcseconds (mas) per year, which we define as the shift in position between consecutive epochs, normalized to one year, and averaged over all consecutive pairs of epochs. The 20 unclassified objects have position change rates below 3 mas yr^{-1}, while objects that belong to Serpens or W40 clearly show larger values because of the significant contribution of their parallax and proper motion. We identify these 20 objects as background sources and assign them a "B" flag in Column 3 of Table 3. Note that not all of these sources are necessarily extragalactic. Some might be Galactic objects located behind the Serpens/Aquila complex. For example, the fit to the positions of the source PMN 1829+0101 yields a distance of $4.025^{+0.854}_{-0.600}$ kpc (Section 3.3). The large number of background sources detected here with the VLBA is not surprising. Oliveira et al. (2009) determined that 25% of the YSO candidates with IR excess in the Serpens/Aquila complex are actually background giants. As stated by these authors, this is consistent with the location of the regions being close to the Galactic plane.

Only eight VLBA-detected objects are previously known YSOs, and one more object is a B1V star. Out of these nine objects, two are resolved into double components in the GOBELINS data, while seven are single stars. This gives a total of 11 individual objects. The astrometry of five single stars is given in the present section; the other two single objects will be presented in a later paper because they were not detected often enough to do astrometric fits. The two binaries are discussed in Section 3.2.

Parallax, ϖ, position at median epoch, (α_0, δ_0), and proper motions μ_α and μ_δ are derived by fitting the equations

$$\alpha(t) = \alpha_0 + (\mu_\alpha \cos\delta)t + \varpi_\alpha f_\alpha(t), \quad (1)$$

Table 3
Detected Sources

GBS-VLA Name[a] (1)	Other Identifier (2)	Type of Source (3)	Minimum Flux at 5 GHz (mJy) (4)	Maximum Flux at 5 GHz (mJy) (5)	Minimum Flux at 8 GHz (mJy) (6)	Maximum Flux at 8 GHz (mJy) (7)	log [T_b (K)][c] (8)	SED Class (9)
Serpens Main								
J182854.44+011859.7	⋯	?	⋯		0.26 ± 0.05		>6.4	⋯
J182854.46+011823.7	⋯	B	3.88 ± 0.05		6.04 ± 0.07		8.5	⋯
J182854.87+011753.0	⋯	B	0.21 ± 0.04		0.24 ± 0.07		7.2	⋯
J182903.06+012331.0	⋯	B	0.49 ± 0.05	0.76 ± 0.07	⋯		7.5	⋯
J182905.07+012309.0	⋯	B	0.26 ± 0.04	0.31 ± 0.05	⋯		>6.5	⋯
J182910.17+012559.5	SSTc2d J182910.2+012560	B	2.70 ± 0.05	3.45 ± 0.05	⋯		9.3	⋯
J182911.94+012119.4	⋯	B	0.36 ± 0.03	0.51 ± 0.06	⋯		7.7	⋯
J182916.11+010437.5	SSTSL2 J182916.10+010438.6	B	0.33 ± 0.06		0.24 ± 0.05	0.26 ± 0.08	8.0	⋯
J182918.23+011757.7	SSTc2d J182918.2+011758	B	0.19 ± 0.05	0.25 ± 0.05	⋯		7.3	⋯
J182926.71+012342.1	SSTSL2 J182926.72+012342.4	B	0.17 ± 0.05	0.25 ± 0.06	⋯		6.6	⋯
J182930.71+010048.3	PMN 1829+0101	B	3.87 ± 0.05	7.44 ± 0.10	⋯		8.7	⋯
J182933.07+011716.3	GFM 11	YSO	0.19 ± 0.04		0.27 ± 0.05	0.33 ± 0.06	>6.6	Class III
J182935.02+011503.2	DCE08-210 5	B	0.14 ± 0.05	0.20 ± 0.04	⋯		>6.3	⋯
J182936.50+012317.0	SSTc2d J182936.5+012317	B	0.14 ± 0.04	0.26 ± 0.05	⋯		>6.4	⋯
J182944.07+011921.1	NVSS 182944+011920	B	1.41 ± 0.04	1.74 ± 0.04	⋯		>7.2	⋯
J182948.83+010647.4	SSTc2d J182948.8+010648	B	0.35 ± 0.05		0.63 ± 0.07		7.5	⋯
J182949.50+011955.8	⋯	B	1.96 ± 0.07	2.40 ± 0.07	⋯		7.6	⋯
J182951.04+011533.8	ETC 8	B	0.35 ± 0.06	0.59 ± 0.05	⋯		8.0	⋯
J182957.89+011246.0	EC 95A	YSO	0.26 ± 0.05	1.18 ± 0.04	⋯		8.3	P-HAeBe
J182957.89+011246.0	EC 95B		0.16 ± 0.04	1.17 ± 0.04	⋯		8.4	
J182957.89+011246.0	EC 95C[b]		⋯	⋯	0.86 ± 0.19	3.68 ± 0.10	>7.4	
J183000.65+011340.0	GFM 65A	YSO	0.26 ± 0.05	0.50 ± 0.04	⋯		>6.7	Class III
J183000.65+011340.0	GFM 65B		0.22 ± 0.05	0.57 ± 0.11	⋯		6.4	
J183004.62+012234.1	GFM 70	B	0.41 ± 0.05	0.42 ± 0.05	⋯		>6.6	⋯
J182952.73-015159.9	⋯	B	0.20 ± 0.05	0.26 ± 0.07	⋯		6.6	⋯
W40								
J183044.11-020145.6	2M18304408–0201458	B	1.65 ± 0.06	2.15 ± 0.06	⋯		7.9	⋯
J183114.82-020350.1	KGF 36	Star	0.41 ± 0.08	0.48 ± 0.05	0.36 ± 0.09	0.48 ± 0.08	7.3	⋯
J183118.68-015455.9	⋯	B	0.43 ± 0.10	0.52 ± 0.06	1.14 ± 0.18		7.0	⋯
J183122.32-020619.6	KGF 82	YSO	0.41 ± 0.05		0.26 ± 0.06		7.6	Class III
J183123.62-020535.8	KGF 97	YSO	0.10 ± 0.05	1.21 ± 0.05	⋯		7.9	Class III
J183126.02-020517.0	KGF 122	YSO	0.20 ± 0.05	0.91 ± 0.06	⋯		8.0	Class II
J183127.45-020512.0	KGF 133	YSO	0.45 ± 0.07	0.51 ± 0.06	2.40 ± 0.11		7.7	Class II/III
J183127.65-020509.7	KGF 138	YSO	0.35 ± 0.06		⋯		>6.5	HAeBe

Notes.
[a] GBS-VLA stands for Gould's Belt Very Large Array Survey (Ortiz-León et al. 2015).
[b] Data corresponding to EC 95C were taken as part of projects BL160 and BD155, and are shown here for completeness.
[c] Because most of the sources show significant flux variations, this value corresponds to the maximum brightness temperature.

Table 4
Measured Positions of EC 95

Julian Day	Project[a]	α (J2000.0)	σ_α	δ (J2000.0)	σ_δ
EC 95A					
2454800.39885	BL160	18 29 57.89186638	0.00000180	1 12 46.110101	0.000069
2454890.14136	BL160	18 29 57.89217322	0.00000048	1 12 46.106940	0.000018
2455171.38315	BL160	18 29 57.89222331	0.00000098	1 12 46.095333	0.000041
2455268.11855	BL160	18 29 57.89247995	0.00000202	1 12 46.092081	0.000067
2455356.87555	BL160	18 29 57.89242962	0.00000117	1 12 46.089683	0.000054
2455936.29042	BD155	18 29 57.89251865	0.00000457	1 12 46.068868	0.000150
2455937.28769	BD155	18 29 57.89253227	0.00000298	1 12 46.068531	0.000082
2456522.68545	BD155	18 29 57.89239849	0.00000095	1 12 46.053528	0.000034
2456524.67999	BD155	18 29 57.89238944	0.00000228	1 12 46.053868	0.000114
2456538.70634	BL175	18 29 57.89232999	0.00000204	1 12 46.054528	0.000066
2456720.20849	BL175	18 29 57.89263275	0.00000445	1 12 46.049701	0.000122
2456943.59865	BL175	18 29 57.89233271	0.00000528	1 12 46.043694	0.000186
2457507.02912	BL175	18 29 57.89266020	0.00000104	1 12 46.032795	0.000036
EC 95B					
2454457.31822	BL156	18 29 57.89095609	0.00000120	1 12 46.107905	0.000038
2454646.81935	BL160	18 29 57.89095848	0.00000481	1 12 46.107242	0.000186
2454724.60637	BL160	18 29 57.89080948	0.00000083	1 12 46.105900	0.000029
2454800.39885	BL160	18 29 57.89088405	0.00000217	1 12 46.104416	0.000089
2454890.14136	BL160	18 29 57.89112095	0.00000388	1 12 46.103859	0.000138
2454985.89100	BL160	18 29 57.89106970	0.00000414	1 12 46.104177	0.000240
2455074.64800	BL160	18 29 57.89091190	0.00000082	1 12 46.103134	0.000032
2455268.11855	BL160	18 29 57.89131814	0.00000402	1 12 46.100962	0.000162
2455356.87555	BL160	18 29 57.89128563	0.00000363	1 12 46.101013	0.000176
2455442.64072	BL160	18 29 57.89116731	0.00000472	1 12 46.099877	0.000202
2455936.29042	BD155	18 29 57.89185545	0.00000614	1 12 46.091786	0.000156
2456522.68545	BD155	18 29 57.89246953	0.00000063	1 12 46.081657	0.000023
2456524.67999	BD155	18 29 57.89246863	0.00000421	1 12 46.081514	0.000137
2456538.70634	BL175	18 29 57.89244323	0.00000760	1 12 46.081859	0.000200
2456720.20849	BL175	18 29 57.89295395	0.00000877	1 12 46.078949	0.000243
2456943.59865	BL175	18 29 57.89292358	0.00000378	1 12 46.072521	0.000108
2457084.21205	BL175	18 29 57.89339762	0.00000179	1 12 46.068654	0.000071
2457302.61352	BL175	18 29 57.89339468	0.00000865	1 12 46.063242	0.000279
2457391.30720	BD155	18 29 57.89364862	0.00000016	1 12 46.060099	0.000006
2457507.02912	BL175	18 29 57.89389465	0.00000108	1 12 46.058656	0.000036
EC 95C					
2454724.60637	BL160	18 29 57.89856745	0.00000305	1 12 46.205651	0.000108
2455936.29042	BD155	18 29 57.89945356	0.00000060	1 12 46.166823	0.000019

Note.
[a] VLBA project code.

$$\delta(t) = \delta_0 + \mu_\delta t + \varpi_\delta f_\delta(t), \tag{2}$$

to the measured positions and separately minimizing χ^2_α and χ^2_δ along the R.A. and decl. directions, respectively. Here, f_α and f_δ are the projections of the parallactic ellipse over α and δ, respectively. The values of the parallax determined in R.A. (ϖ_α) and decl. (ϖ_δ) were then weighted-averaged to produce a single parallax value. The fit is then repeated to solve for the remaining parameters while holding the best-fit parallax solution constant. We show the resulting best fits in Figure 4 and summarize the derived astrometric parameters in Table 5. Errors in the model parameters depend on the positional uncertainties of all the individual detections as measured by JMFIT. However, systematic offsets in positions could be introduced by errors in station coordinates, Earth rotation parameters, reference source coordinates, and tropospheric zenith delays (Pradel et al. 2006). When data from many epochs are available, these systematic offsets can be estimated by scaling the positional errors provided by JMFIT until the reduced χ^2 of the fit becomes equal to 1 (e.g., Menten et al. 2007). Here we are not able to apply this approach given that we typically have three to four epochs available for each source. We thus estimate systematic errors by using the empirical relations found by Pradel et al. (2006), according to which the VLBA astrometric accuracy scales linearly with the target to reference source angular separation. We obtain $\Delta\alpha \cos\delta = 0.052$–$0.070$ mas and $\Delta\delta = 0.124$–0.182 mas by extrapolating the astrometric errors given in Tables 3 and 4 in Pradel et al. (2006) for a source at a decl. of 0° (the range in errors corresponds to the different source to calibrator angular separations). In order to estimate the offsets introduced by ionospheric phase delays, we follow the approach outlined in Kounkel et al. (2017). Source positions were referenced to a secondary phase calibrator by adding offsets such that the

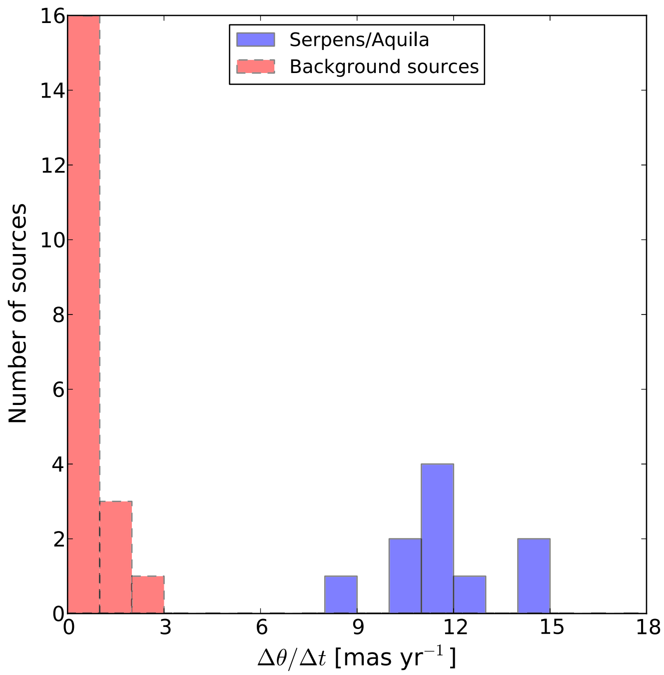

Figure 3. Histogram of position change rate for all sources detected at least twice toward Serpens/Aquila. The sources previously identified as members of the complex are shown as a blue histogram. These are 10 sources: 5 single YSOs, the 4 components of the two binary systems, and the B1V star. The source KGF 138 is not shown because it has been detected only once. Other sources, whose classification is unknown in the literature, are shown as a red histogram.

position of this secondary calibrator remains fixed in all epochs. We repeat the astrometric fits to the re-referenced target positions, obtaining a different solution to that derived when all positions are referenced to the main phase calibrator. We take the difference in the distance solutions divided by the angular separation between the two phase calibrators as the phase gradient across the sky introduced by ionospheric delays. On average, this yields additional systematic offsets of $\Delta\alpha\cos\delta = 0.026$ mas and $\Delta\delta = 0.042$ mas in decl. In total, systematic errors of $\Delta\alpha\cos\delta = 0.058$–$0.075$ mas and $\Delta\delta = 0.130$–0.187 mas were added quadratically to the statistical errors provided by JMFIT at each individual epoch and used in the last iteration of the fits.

We discuss separately the properties of these objects in the following sections. Sources names come from the X-ray surveys by Giardino et al. (2007, GFM) and Kuhn et al. (2010, KGF).

3.1.1. GFM 11 = GBS-VLA J182933.07+011716.3

GFM 11 is a Class III YSO (Giardino et al. 2007). Its spectral type remains somewhat uncertain: between G2.5 (Winston et al. 2010) and K0 (Erickson et al. 2015). The source has a spectral index[13] of $+0.3 \pm 0.2$, and shows high levels of variability in both VLA (>73%; Ortiz-León et al. 2015) and VLBA observations. Based on optical spectroscopy, Erickson et al. (2015) estimated a mass of 2.0 $M_\odot$ for the source.

[13] From VLA measurements published in Ortiz-León et al. (2015). The spectral index was taken between 4.5 and 7.5 GHz.

3.1.2. KGF 36 = GBS-VLA J183114.82-020350.1

This source, identified as a main sequence star of B1 spectral type by Shuping et al. (2012), is located in the W40 cluster. Its radio flux as measured by the VLA shows variations of $44 \pm 9\%$ on timescales of months at 4.5 GHz, and it has a spectral index of $+0.3 \pm 0.2$. Shuping et al. (2012) also suggested that KGF 36 is probably a binary source due to the presence of strong He I 1.083 μm absorption in the star spectra. However, our VLBA observations have detected a single source with no sign of a close companion in the parallax fit. Non-thermal emission has been confirmed in other early-type B stars. The source S1 in Ophiuchus (Andre et al. 1988) is perhaps the most documented case. Kuhn et al. (2010) derived a photometric mass of 17 $M_\odot$ from a color–magnitude J versus $J - H$ diagram assuming distance of 600 pc and age of 1 Myr.

3.1.3. KGF 97 = GBS-VLA J183123.62-020535.8

KGF 97, whose spectral type is unknown, is a YSO also located in the W40 cluster. Since the source does not show excess in the infrared K_s band, it is classified as a Class III object, with a mass of 3.3 ± 1.0 $M_\odot$ (Kuhn et al. 2010; reduced by a factor of ~2 given a distance of 436 pc). The source is found to be very variable in our VLBA observations by a factor >10. Additionally, it is one of the few sources of the cluster detected in circular polarization (Ortiz-León et al. 2015), a strong signature of gyrosynchrotron radiation. The spectral index is -0.1 ± 0.1.

3.1.4. KGF 122 = GBS-VLA J183126.02-020517.0

This source was classified as a low-mass Class II YSO by Shuping et al. (2012) based on the analysis of infrared data. It shows high flux variations in both VLA ($52 \pm 5\%$ at 4.5 GHz) and VLBA observations, and has a negative spectral index of -0.6 ± 0.2. Kuhn et al. (2010) estimated a photometric mass of 16 $M_\odot$ for the source and a bolometric luminosity of $2.9 \times 10^4 L_\odot$, assuming 600 pc as the distance to the cluster (a lower distance of 436 pc reduces the luminosity and mass by a factor of ~2). Thus, the source may be associated with an early-type source. We discard the last measured source position for the derivation of the astrometric parameters because it significantly deteriorates the quality of the fit and, since we ignore the source of any positional error that may be introduced in this particular epoch, we cannot correct the source position.

3.1.5. KGF 133 = GBS-VLA J183127.45-020512.0

KGF 133 was identified as a Class II/III YSO by Mallick et al. (2013) based on *Spitzer* and near-IR data. Like the rest of the VLBA-detected YSOs, the source is very variable in radio, with fluctuations of $96 \pm 1\%$ at 4.5 GHz (Ortiz-León et al. 2015). The spectral index of the source is $+0.3 \pm 0.2$. The mass of the source is not yet well constrained. Kuhn et al. (2010) derived a photometric mass of 24 $M_\odot$ (reduced to ~12 $M_\odot$ for a distance of 436 pc), but the associated error is uncertain and not provided by these authors.

3.2. Multiple Systems

3.2.1. GFM 65 = GBS-VLA J183000.65+011340.0

This source is an M0.5, 0.96 $M_\odot$ star (Winston et al. 2010) located in the Serpens Core. It was classified as a Class III

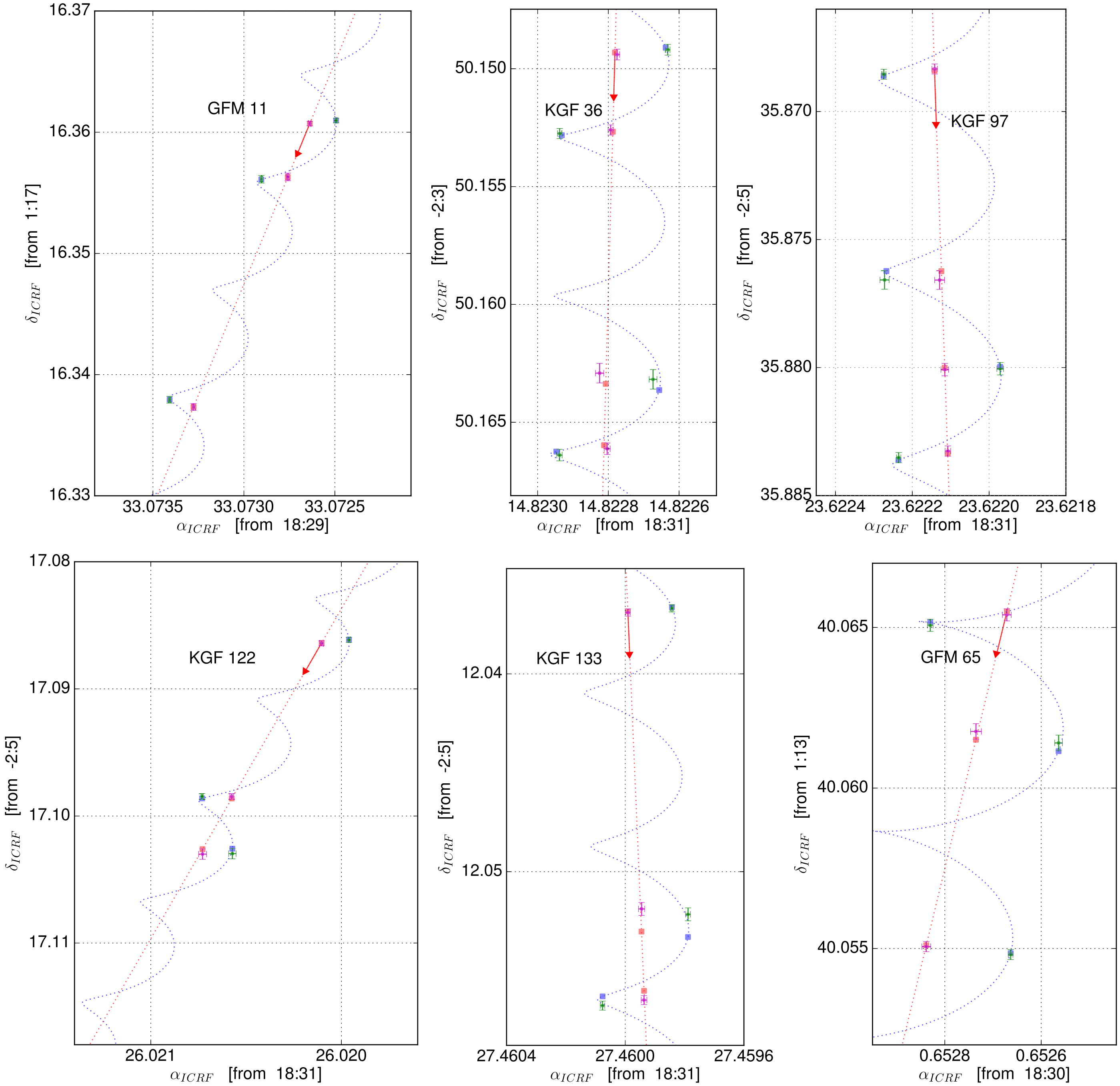

Figure 4. Observed positions and best fits for six sources. Measured positions are shown as green dots, and expected positions from the fits as blue squares. The blue dotted line is the full model, and the red line is the model with the parallax signature removed. The red squares indicate the position of the source expected from the model without parallax, while magenta dots are measured positions with parallax signature removed. The arrow indicates the direction of position change with time.

object by Giardino et al. (2007). Based on multi-epoch VLA observations, Ortiz-León et al. (2015) found that the source shows large flux variations (>75%) on timescales of months, and measured a spectral index of -0.9 ± 0.4. Both properties of the radio emission are fully consistent with its non-thermal nature. Because of this variability, the source has been detected with the VLBA just in three of the six observed epochs. Another source, possible a gravitationally bound companion, was detecetd in two epochs separated by ~5 mas from the primary. We are not able to constrain the orbit of the system using our current small number of detections. We perform the parallax fit for only one component following the procedure described in Section 3.1.

3.2.2. EC 95 = GBS-VLA J182957.89+011246.0

EC 95 is located in the Serpens core. The system is formed by two close components first observed by Dzib et al. (2010). Early estimations of its spectral type (~K2 star), age (~10^5 years), and mass (~4 $M_\odot$) indicated that the source is a proto-Herbig AeBe star (Preibisch 1999). Dzib et al. (2011) reported observations from 11 epochs taken with the VLBA at 8 GHz

Table 5
Parallaxes and Proper Motions

GBS-VLA Name (1)	Other Identifier[a] (2)	Parallax (mas) (3)	$\mu_\alpha \cos\delta$ (mas yr^{-1}) (4)	μ_δ (mas yr^{-1}) (5)	Distance (pc) (6)
J182933.07+011716.3	GFM 11	2.313 ± 0.078	3.634 ± 0.050	−8.864 ± 0.127	432.3 ± 14.6
J182957.89+011246.0	EC 95	2.291 ± 0.038	3.599 ± 0.026	−8.336 ± 0.030	436.4 ± 7.1
J183000.65+011340.0	GFM 65[b]	2.638 ± 0.118	1.573 ± 0.070	−6.513 ± 0.152	379.1 ± 17.0
J183114.82-020350.1	KGF 36	2.302 ± 0.063	0.186 ± 0.053	−6.726 ± 0.121	434.5 ± 11.8
J183123.62-020535.8	KGF 97	2.186 ± 0.076	−0.258 ± 0.058	−7.514 ± 0.135	457.5 ± 16.0
J183126.02-020517.0	KGF 122	2.372 ± 0.120	4.586 ± 0.074	−7.946 ± 0.167	421.5 ± 21.4
J183127.45-020512.0	KGF 133	2.385 ± 0.098	−0.330 ± 0.049	−7.746 ± 0.111	419.3 ± 17.3

Notes.
[a] GFM—Giardino et al. (2007); EC—Eiroa & Casali (1995), KGF—Kuhn et al. (2010).
[b] Parallax solution could be affected by unmodeled binary motion.

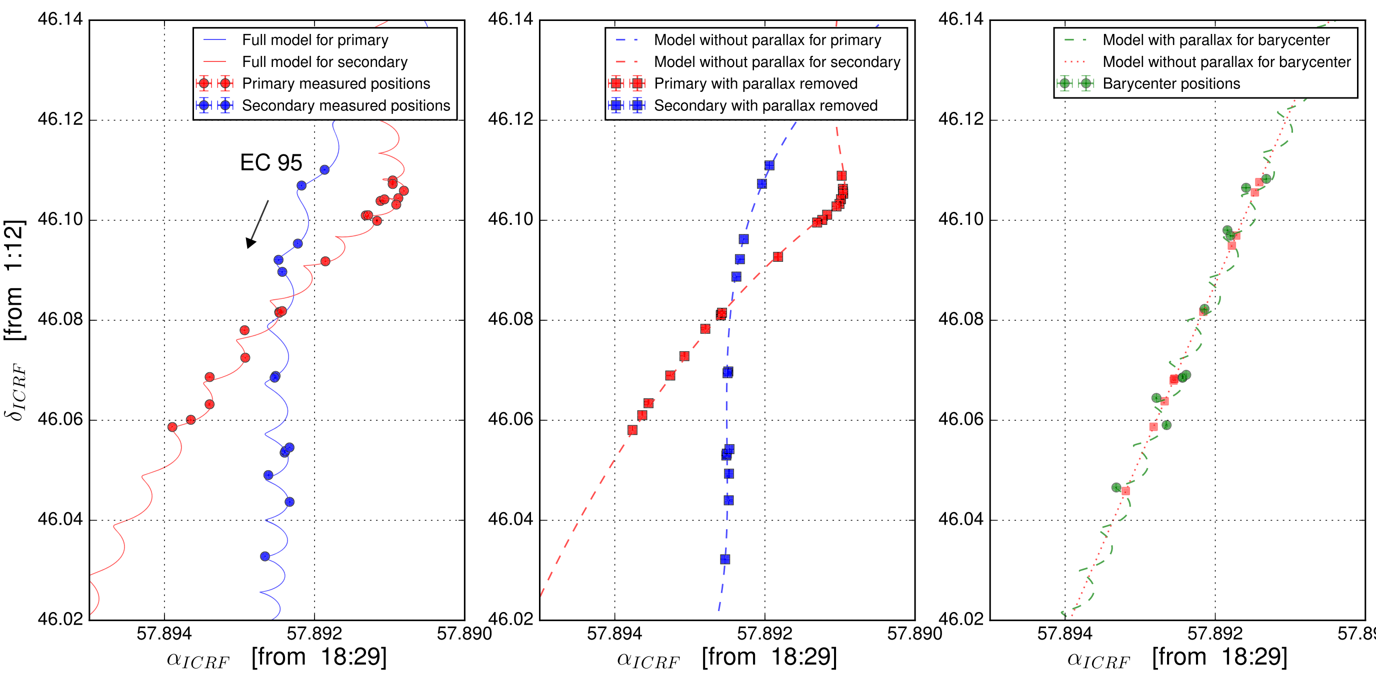

Figure 5. Observed positions of EC 95 and best astrometric fits. Left: measured positions of each component are shown as red and blue circles. The solid lines show the fit corresponding to the "Full model" described in the text. The arrow indicates the direction of position change with time. Middle: the squares mark the measured positions with the parallax signature removed, while the dashed lines are the fits from the "Full model," also without parallax. Right: green dots mark the position of the center of mass derived using the solutions from the orbital model for the mass ratio. The green dashed line is the model for the motion of the center of mass of the system, while the red line is this same model with the parallax signature removed. The red squares indicate the position of the center of mass expected from the model without parallax.

and reported a distance to the source of 429 ± 2 pc. Earlier, Dzib et al. (2010) performed a circular Keplerian orbit fit to the data from 8 of these 11 epochs, constraining the orbital period of the system to 10–20 years.

In order to derive the full orbital parameters of EC 95, we carried out follow-up VLBA observations as part of the project coded BD155, which observed the system at 8 GHz in five new epochs. The source has also been monitored with GOBELINS at 5 GHz, and six additional epochs are available. The new observations together with those previously reported by Dzib et al. (2011) cover a baseline timescale of ∼8 years, i.e., a significant fraction of the orbit. Old data were recalibrated by homogeneously applying the same calibration strategy as for the new data, and combined with the GOBELINS observations to form a single data set. The data were fitted with two models. In the first "Full model," we fit the orbital and astrometric parameters of the system simultaneously. Orbital elements in this model are period (P), time of periastron passage (T), eccentricity (e), angle of line of nodes (Ω), inclination (i), angle from node to periastron (ω), semimajor axis (a_1) of the primary, and mass ratio (m_2/m_1). Astrometric parameters include center of mass at the first epoch of the GOBELINS observations where the primary is detected ($\alpha_{\rm CM,0}$, $\delta_{\rm CM,0}$), parallax (ϖ), and proper motion (μ_α, μ_δ) of the system. For this fit, a grid of initial guesses of P, e, T, and ω is explored. The final values of these parameters are fine-tuned by the code, and the

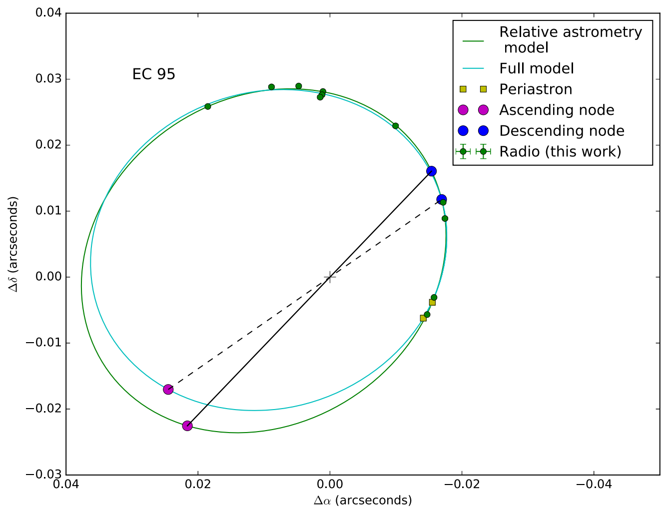

Figure 6. Relative positions of the components of the young binary system EC 95. The green points mark the detections with the VLBA. Green and cyan solid lines correspond to the "Relative astrometry" and "Full model" orbital fits, respectively. The black solid and dashed lines trace the line of nodes of the "Relative astrometry" and "Full model," respectively.

remaining model parameters are fitted directly. The first panel of Figure 5 shows the resulting best-fit curve and the measured positions of both components of the system, while the second panel shows the same fit without parallax and measured positions with parallax signature removed. Finally, the motion of the barycenter is shown in the last panel of the same figure.

In the second "Relative Model," we use the *Binary Star Combined Solution Package* (Gudehus 2001) to fit the positions of the secondary relative to the primary component and solve for P, T, e, Ω, i, ω, and a. The total mass of the system is then derived from Kepler's law. The solutions found by the "Full model" are used as initial guesses for this fit. Uncertainties in the orbital elements are computed from the scatter on model parameters. The best-fit solution is shown in Figure 6 and compared with the solution found by the "Full model." Solutions for the orbital elements from both models are given in Table 6. Dzib et al. (2010) argued that one of the system components should be considerably more massive than the other; however, their reported observations only covered a small fraction of the complete orbit. Here, based on a larger number of observations, we have derived a similar mass for both components, while the total mass of $\sim 4 M_\odot$ is consistent with that estimated in past works (Preibisch 1999; Pontoppidan et al. 2004) and with the spectral type of the source.

A third source is detected in the EC95 system at two epochs at 8 and 61σ, respectively. This source was located ∼145 mas to the northeast of the barycenter of the close binary, at a position angle of 48°.3 on 2008 September 15, and ∼138 mas in the same direction, at a position angle of 52°.4 on 2012 January 9 (see Table 4). The third source was also detected in near-IR (NIR) observations taken at the VLT on 2005 May 11 and 22 (Duchêne et al. 2007). A map of the system as seen in NIR emission is shown in the first panel of Figure 7. The northernmost source is EC 92, a young ($\sim 10^5$ years), Class I (Pontoppidan et al. 2004) and low-mass ($\sim 0.5\ M_\odot$; Preibisch 1999) star. EC 95 is the brightest source to the south in the map. While the two close components of EC 95 are unresolved, the third component is clearly visible, at a position angle of 47°.2 and separation of 152 mas from the close binary, i.e., at a position similar to that of the radio source seen in our VLBA images (Figure 7, right). Given the short angular separation of the third component relative to the close binary, it is possible that the three sources form a bound system. To investigate this possibility, we include two more free parameters in the "Full model," corresponding to the acceleration terms in R.A., a_α, and decl., a_δ. We find that these acceleration terms are zero within the errors, and that the motion of the barycenter of the close binary remains linear during the timescale covered by our observations. This suggests that the third source may be much less massive than the close binary and following a very long period orbit. Actually, if we assume that the total mass of the system is 4.2 $M_\odot$, i.e., that the mass of the third source is negligible, we estimate an orbital period ∼260 years. The change in angular separation of the third companion (detected first in the NIR and then in the VLBA images) relative to the barycenter of the close binary is ∼20 mas in 6.7 years, while the position angle only changes ∼5° over this timescale. This is consistent, within the errors, with the expected motion of the companion on a circular orbit that has the period estimated above. Unfortunately, the third companion has remained undetectable in the radio since 2012. If there were more detections, we could constrain its astrometric parameters and investigate a possible acceleration induced by its orbital motion around the close binary.

Finally, we note that Dzib et al. (2011) estimated a distance to EC 95 of 429 ± 2 pc by separately modeling the source motion of each component as a superposition of parallax and uniform accelerated proper motion. The derived distance from the "Full model" is 435.2 ± 6.0 pc, which is consistent within 1σ with the previous determination.

3.3. Comments on Other Sources: PMN 1829+0101

PMN 1829+0101 = GBS VLA J182930.71+010048.3 is a strong radio source with reported VLA fluxes of 196.0 ± 5.9 mJy at 1.4 GHz (Ofek & Frail 2011) and 32.10 ± 5.60 mJy at 4.5 GHz (Ortiz-León et al. 2015). The source shows an extended structure of ∼1″.4 in the 4.5 GHz VLA images, but this emission is filtered out by the VLBA. There is a counterpart in X-ray emission at ∼1″.3 (XMM-

Table 6
Orbital Elements of EC 95

Model	a	P	T_0	e	Ω	i	ω	M_1	M_2	M_T
	(mas)	(years)			(°)	(°)	(°)	($M_\odot$)	($M_\odot$)	($M_\odot$)
(1)	(2)	(3)	(4)	(5)	(6)	(7)	(8)	(9)	(10)	(11)
Full	28.9 ± 0.4	21.5 ± 1.5	2008.85 ± 2.0	0.397 ± 0.001	124.8 ± 2.1	31.6 ± 0.9	477.5 ± 1.8	2.0 ± 0.2	2.3 ± 0.1	4.3 ± 0.2
Rel. astr.	30.7 ± 1.4	23.1 ± 1.4	2009.08 ± 0.14	0.393 ± 0.011	136.2 ± 2.5	34.8 ± 2.0	475.3 ± 2.8	⋯	⋯	4.5 ± 0.2

Table 7
Measured Source Positions

Julian Day	α (J2000.0)	σ_α	δ (J2000.0)	σ_δ
		SSTc2d J182910.2+012560		
2456537.71083	18 29 10.18111439	0.00000048	1 25 59.593986	0.000016
2456718.21396	18 29 10.18111515	0.00000048	1 25 59.593964	0.000016
2456938.61153	18 29 10.18111964	0.00000046	1 25 59.594012	0.000016
2457081.21921	18 29 10.18110324	0.00000063	1 25 59.594051	0.000020
2457300.62039	18 29 10.18110850	0.00000051	1 25 59.594058	0.000017
		SSTc2d J182918.2+011758		
2456537.71083	18 29 18.23057894	0.00000623	1 17 57.783157	0.000237
2456718.21396	18 29 18.23057676	0.00000432	1 17 57.782977	0.000165
2456938.61153	18 29 18.23060031	0.00000827	1 17 57.783177	0.000266
2457081.21921	18 29 18.23056481	0.00000605	1 17 57.782967	0.000199
2457300.62039	18 29 18.23058354	0.00000919	1 17 57.783323	0.000305
		GBS-VLA J182903.06+012331.0		
2456537.71083	18 29 03.06984956	0.00000319	1 23 31.087749	0.000103
2456718.21396	18 29 03.06986038	0.00000339	1 23 31.087530	0.000110
2456938.61153	18 29 03.06986699	0.00000383	1 23 31.087498	0.000101
2457081.21921	18 29 03.06987411	0.00000425	1 23 31.087780	0.000116
2457300.62039	18 29 03.06987273	0.00000382	1 23 31.087686	0.000132
		SSTc2d J182936.5+012317		
2456537.71083	18 29 36.50110691	0.00000859	1 23 17.076353	0.000169
2456718.21396	18 29 36.50114312	0.00000627	1 23 17.075662	0.000226
2456938.61153	18 29 36.50113297	0.00000496	1 23 17.076045	0.000161
2457081.21921	18 29 36.50112373	0.00001097	1 23 17.075484	0.000410
2457300.62039	18 29 36.50110998	0.00000771	1 23 17.076210	0.000196
		GBS-VLA J182905.07+012309.0		
2456537.71083	18 29 05.08095263	0.00000445	1 23 09.149373	0.000137
2456718.21396	18 29 05.08096153	0.00000384	1 23 09.149402	0.000155
2457081.21921	18 29 05.08094750	0.00000559	1 23 09.149718	0.000160
2457300.62039	18 29 05.08094627	0.00000762	1 23 09.150555	0.000146
		SSTSL2 J182926.72+012342.4		
2456537.71083	18 29 26.71049982	0.00000918	1 23 42.131201	0.000268
2456718.21396	18 29 26.71050367	0.00001050	1 23 42.130807	0.000385
		GBS-VLA J182911.94+012119.4		
2456537.71083	18 29 11.94832584	0.00000362	1 21 19.484862	0.000107
2456718.21396	18 29 11.94830530	0.00000283	1 21 19.485004	0.000112
2456938.61153	18 29 11.94832429	0.00000313	1 21 19.484997	0.000106
2457081.21921	18 29 11.94830236	0.00000478	1 21 19.485052	0.000132
2457300.62039	18 29 11.94833353	0.00000291	1 21 19.484955	0.000089
		NVSS 182944+011920		
2456537.71083	18 29 44.07658313	0.00000075	1 19 21.164119	0.000025
2456718.21396	18 29 44.07657402	0.00000085	1 19 21.164280	0.000028
2456938.61153	18 29 44.07659031	0.00000068	1 19 21.164227	0.000023
2457081.21921	18 29 44.07657708	0.00000112	1 19 21.164286	0.000035
2457300.62039	18 29 44.07655805	0.00000085	1 19 21.164512	0.000029
		PMN 1829+0101		
2456538.70634	18 29 30.72388371	0.00000033	1 0 48.005138	0.000010
2456720.20849	18 29 30.72391467	0.00000085	1 0 48.005243	0.000022
2456943.59865	18 29 30.72388420	0.00000045	1 0 48.004833	0.000016
		DCE08-210 5		
2456538.70634	18 29 35.02394353	0.00001739	1 15 03.254608	0.000371
2456720.20849	18 29 35.02397943	0.00001364	1 15 03.252858	0.000403
2457507.02912	18 29 35.02401622	0.00000701	1 15 03.253580	0.000198

Table 7
(Continued)

Julian Day	α (J2000.0)	σ_α	δ (J2000.0)	σ_δ
		GFM 65		
2456720.20849	18 30 00.65283020	0.00000429	1 13 40.065067	0.000136
2456943.59865	18 30 00.65256389	0.00000712	1 13 40.061403	0.000205
2457302.61352	18 30 00.65266340	0.00000277	1 13 40.054815	0.000088
second source:				
2456720.20849	18 30 00.65296360	0.00002331	1 13 40.066599	0.000638
2456943.59865	18 30 00.65289182	0.00000696	1 13 40.061476	0.000276
		ETC 8		
2456720.20849	18 29 51.04143717	0.00000565	1 15 33.871396	0.000160
2456943.59865	18 29 51.04141126	0.00000725	1 15 33.870733	0.000178
2457084.21205	18 29 51.04142997	0.00000353	1 15 33.870437	0.000131
2457302.61352	18 29 51.04141829	0.00000270	1 15 33.870371	0.000080
2457507.02912	18 29 51.04142929	0.00000406	1 15 33.870259	0.000106
		KGF 122		
2456539.70380	18 31 26.01996029	0.00000276	−2 5 17.086151	0.000086
2457102.16179	18 31 26.02073064	0.00000306	−2 5 17.098461	0.000137
2457285.66188	18 31 26.02057197	0.00001863	−2 5 17.102963	0.000368
2457448.21552	18 31 26.02087306	0.00001310	−2 5 17.105731	0.000405
		2M18304408–0201458		
2456539.70380	18 30 44.11485642	0.00000199	−2 1 45.688322	0.000051
2456721.20565	18 30 44.11487547	0.00000271	−2 1 45.689938	0.000071
2456946.58954	18 30 44.11484733	0.00000336	−2 1 45.688604	0.000087
2457102.16179	18 30 44.11486486	0.00000140	−2 1 45.688221	0.000038
2457285.66188	18 30 44.11485685	0.00000236	−2 1 45.688281	0.000057
		KGF 138		
2457102.16179	18 31 27.65620135	0.00000709	−2 5 09.799495	0.000178
		KGF 97		
2456721.20565	18 31 23.62227407	0.00000250	−2 5 35.868544	0.000074
2456946.58954	18 31 23.62203557	0.00002812	−2 5 35.873472	0.000761
2457102.16179	18 31 23.62227217	0.00001073	−2 5 35.876576	0.000314
2457285.66188	18 31 23.62197113	0.00000699	−2 5 35.880042	0.000161
2457448.21552	18 31 23.62223545	0.00000309	−2 5 35.883516	0.000086
		KGF 36		
2456543.60141	18 31 14.82263201	0.00000386	−2 3 50.149196	0.000131
2456726.05521	18 31 14.82293762	0.00000369	−2 3 50.152750	0.000106
2457306.96324	18 31 14.82267359	0.00000980	−2 3 50.163179	0.000371
2457448.21552	18 31 14.82293818	0.00000571	−2 3 50.166392	0.000155
		GBS-VLA J182952.73-015159.9		
2456541.69591	18 29 52.73464125	0.00001627	−1 51 59.925315	0.000561
2456723.19777	18 29 52.73465607	0.00002462	−1 51 59.926572	0.000665
2457309.09678	18 29 52.73469573	0.00001149	−1 51 59.925989	0.000363
		KGF 82		
2456543.60141	18 31 22.32975638	0.00000485	−2 6 19.633463	0.000140
2457306.96324	18 31 22.32894475	0.00000404	−2 6 19.660373	0.000166
		KGF 133		
2456543.60141	18 31 27.45984260	0.00000137	−2 5 12.036684	0.000039
2457306.96324	18 31 27.45978832	0.00000657	−2 5 12.052156	0.000273
2457448.21552	18 31 27.46007650	0.00000568	−2 5 12.056771	0.000139
		GBS-VLA J183118.68-015455.9		
2456706.16961	18 31 18.68250486	0.00001724	−1 54 56.073788	0.000262
2457084.21205	18 31 18.68250948	0.00001509	−1 54 56.073322	0.000371

Table 7
(Continued)

Julian Day	α (J2000.0)	σ_α	δ (J2000.0)	σ_δ
2457302.61352	18 31 18.68249661	0.00000858	−1 54 56.072971	0.000207
		GBS-VLA J182949.50+011955.8		
2456541.69877	18 29 49.50633251	0.00000273	1 19 55.885107	0.000090
2456723.20062	18 29 49.50632851	0.00000189	1 19 55.885721	0.000123
2457309.09678	18 29 49.50633154	0.00000120	1 19 55.885384	0.000068
		GFM 70		
2456723.20062	18 30 04.62941667	0.00000502	1 22 34.131415	0.000132
2457309.09678	18 30 04.62940928	0.00000397	1 22 34.131168	0.000121
		GFM 11		
2456543.69416	18 29 33.07249309	0.00000229	1 17 16.360959	0.000098
2456726.19504	18 29 33.07290417	0.00000527	1 17 16.356120	0.000275
2457507.02912	18 29 33.07340833	0.00000593	1 17 16.337928	0.000238
		SSTSL2 J182916.10+010438.6		
2456543.69416	18 29 16.11947301	0.00000517	1 4 37.589379	0.000201
2456726.19504	18 29 16.11946492	0.00000667	1 4 37.589438	0.000220
2457307.60223	18 29 16.11947017	0.00000623	1 4 37.589495	0.000238
		GBS-VLA J182854.46+011823.7		
2456749.07794	18 28 54.46499411	0.00000049	1 18 23.813820	0.000015
2457281.61856	18 28 54.46500889	0.00000023	1 18 23.813619	0.000008
		GBS-VLA J182854.44+011859.7		
2457281.61856	18 28 54.44344643	0.00000226	1 18 59.737811	0.000112
		GBS-VLA J182854.87+011753.0		
2456749.07794	18 28 54.87254346	0.00000603	1 17 53.051049	0.000192
2457281.61856	18 28 54.87253760	0.00000534	1 17 53.051239	0.000208
		SSTc2d J182948.8+010648		
2456749.09635	18 29 48.82981795	0.00000628	1 6 47.450268	0.000181
2457281.61856	18 29 48.82980672	0.00000240	1 6 47.450032	0.000084

Newton Survey Science Centre 2013) and in the IRAC 3.6 μm band (Evans et al. 2003) at ∼1$''$.7 from the radio peak. The fit to the data yields $\varpi = 0.248 \pm 0.044$ mas, corresponding to a distance of $d = 4025^{+854}_{-600}$ pc. Using this distance we derive the location (x, y, z) of the source in the Milky Way. This position is expressed in the rectangular frame centered on the location of the Sun, with the (Ox) axis pointing toward the Galactic Center, the (Oy) axis perpendicular to (Ox) and pointing in the direction of the Galactic rotation, and (Oz) pointing toward the Galactic North Pole. The source coordinates in this system are $(x, y, z) = (3443, 2096, 377)$ pc: it is located in the direction of the Scutum arm, which hosts newly formed OB-type stars, but at 377 pc above the Galactic mid-plane.

4. DISCUSSION

We have derived the distance to seven objects in the Serpens/Aquila complex. The parallaxes for these objects are shown graphically in Figure 8, where we clearly see that sources in Serpens and Aquila share similar values. Proper motions, on the other hand, show a large spread, but this is expected as Serpens and W40 are different clusters. The weighted mean value of the seven parallaxes is $\varpi = 2.32$ mas, with a weighted standard deviation of $\sigma_\varpi = 0.10$ mas. Only the source GMF 65, for which we derive 379.1 ± 17.0 pc, differs from the rest by more than 1σ. As discussed in Section 3.2.1, this source seems to be a binary system, whose orbital motion remains unmodeled because of the low number of detections. Ignoring this source yields a mean weighted parallax of $\varpi = 2.29 \pm 0.05$ mas. This corresponds to a weighted mean distance of $d = 436.0$ pc, with a standard deviation of $\sigma_d = 9.2$ pc. The standard deviation on the mean reflects only the uncertainties in the distance measurements because typical errors on individual distances are larger than 10 pc.

Note that Straižys et al. (2003) determined the near edge of the Aquila/Serpens cloud complex to be at 225 ± 55 pc, with a depth of 80 pc. Therefore, according to their estimates, the far edge of the complex lies at a distance (assuming a +1σ deviation) of 225 + 55 + 80 = 360 pc (Winston et al. 2010). Assuming a +3σ deviation, we place the far edge of the cloud at a maximum distance of 470 pc, which is consistent with the mean distance to the cloud obtained here from parallax measurements.

Our measurements not only confirm the early estimation by Dzib et al. (2010) of a larger distance to Serpens than previously thought, but also show that Serpens and W40 are

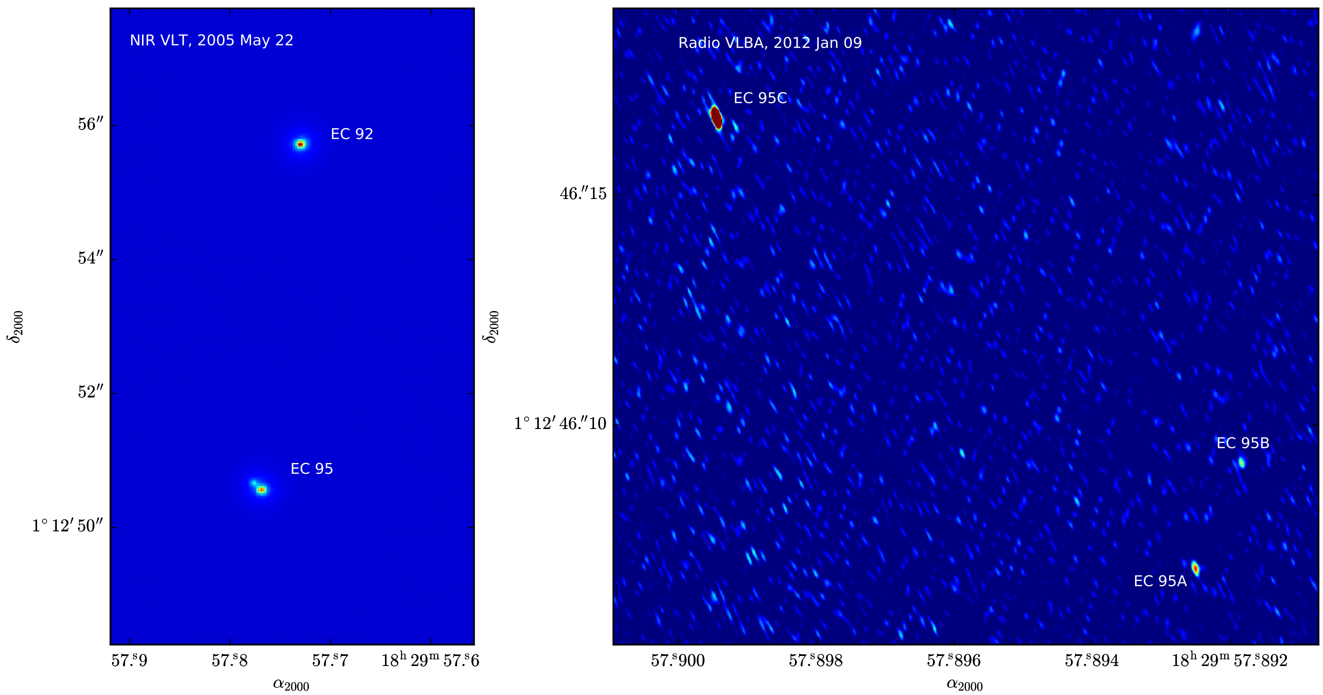

Figure 7. Left: NIR image of EC 92 and EC 95 taken with the VLT. Right: radio image of the system EC 95 corresponding to one of the two epochs when the three sources are detected simultaneously with the VLBA.

part of the same complex, lying at the same distance along the line of sight. Earlier estimates based on indirect methods, e.g., by Kuhn et al. (2010) and Shuping et al. (2012), suggested a mean distance to W40 of $\sim 500 \pm 50$ pc. Based on these measurements, W40 and the Serpens region have been treated in the literature as separate objects, as such works used the value obtained by Straižys et al. (1996) of $\sim$260 pc for the Serpens/Aquila Rift (see, e.g., Straižys et al. 2003; Gutermuth et al. 2008). When it was first discovered, Serpens South was associated with Serpens Main because both regions share similar local standard of rest (LSR) velocities ($\sim$6–11 km s^{-1}; White et al. 1995; Gutermuth et al. 2008; Bontemps et al. 2010), indicating that they are comoving. Until recently, it has become more common to consider that Serpens South and W40 form a single cloud structure. This is because the LSR velocities measured by molecular line observations in the entire W40/Serpens South region are 4–10 km s^{-1} (Zeilik & Lada 1978; Maury et al. 2011), which are in the range of the LSR velocities measured in Serpens Main. We do not have any astrometric measurement to sources in Serpens South (because known YSOs in the cluster are intrinsically radio weak; Ortiz-León et al. 2015; Kern et al. 2016), but given its proximity and similarity in LSR velocities to W40, we speculate that these two clusters are physically associated. If this last statement is confirmed, it would represent meaningful evidence for association among Serpens Main, W40, and Serpens South.

Proper motions are plotted in Figure 8 after the correction for the solar peculiar motion is applied. Mean values are ($\mu_\alpha \cos\delta = 8.0 \pm 2.2$ mas yr^{-1},$\mu_\delta = -11.6 \pm 2.9$ mas yr^{-1}) for Serpens sources and ($\mu_\alpha \cos\delta = 3.8 \pm 4.1$ mas yr^{-1}, $\mu_\delta = -10.2 \pm 0.9$ mas yr^{-1}) for W40 sources. Uncertainties in the mean values correspond to the standard deviation of individual measurements in each cluster. It appears that the clusters are moving in similar directions, which is an additional support for our interpretation of Serpens Main and W40 being part of the same cloud complex.

Finally, we note that a larger distance to the Serpens and Aquila regions imply luminosities and dust masses larger by a factor of $\sim$2.8 relative to those derived assuming 260 pc, and makes YSOs younger with respect to evolutionary tracks. This implies that the physical interpretation of the stellar and core population in the regions needs to be revised.

5. SUMMARY

We have analyzed multi-epoch VLBA observations taken as part of the GOBELINS project toward young stars in the Serpens and W40 regions in the Aquila complex. The astrometric fits to seven sources, including one confirmed binary (posible triple) system, provide us with parallaxes and proper motions for single sources, as well as with the orbital parameters for the multiple system. Since individual parallaxes of sources in Serpens are consistent with those of W40 sources, we conclude that both Serpens and W40 are located at the same distance. The mean parallax value yields 436.0 ± 9.2 pc, confirming the early distance estimation obtained solely for the source EC 95 in the Serpens Core, which was also derived from a parallax measurement with the VLBA. The other 20 sources detected during the survey turned out to be background sources, and not associated with the Aquila Rift.

G.N.O.-L., L.L., L.F.R., G.P., and J.L.R. acknowledge CONACyT, Mexico for financial support through grants 339802, 104497, and 153522. L.L. was supported by DGAPA, UNAM grant IG100913. L.L. and G.N.O.-L. also acknowledge support from von Humboldt Stiftung. N.J.E. was supported by NSF grant AST-1109116 to the University of Texas at Austin. P.A.B.G. acknowledges financial support from FAPESP. The National Radio Astronomy Observatory is operated by

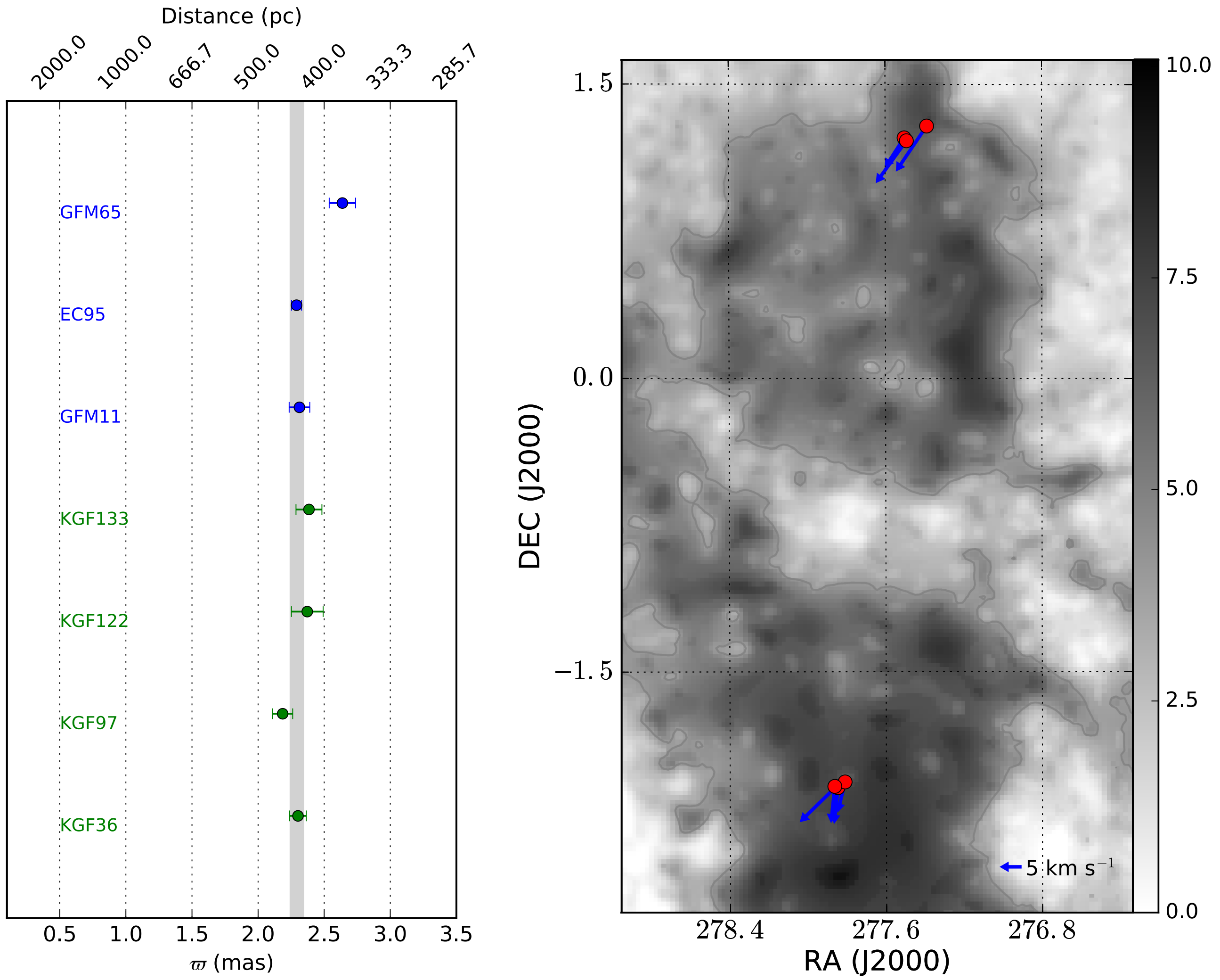

Figure 8. Left: parallax results for the Serpens/Aquila complex. The blue circles and characters are for sources in the Serpens Core, while green circles and characters are for sources W40. The gray vertical bar shows the mean parallax value for all sources except GFM 65 (a binary source for which we are not able to model its orbital motion based on the data collected so far), and its standard deviation (see text). Right: enlargement of Figure 1 showing the spatial distribution of the YSOs in Serpens and W40 with astrometric parameters derived in this work. The arrows represent the source tangential velocity corrected by the solar motion.

Associated Universities, Inc., under cooperative agreement with the National Science Foundation.

REFERENCES

André, P., Men'shchikov, A., Bontemps, S., et al. 2010, A&A, 518, L102
Andre, P., Montmerle, T., Feigelson, E. D., Stine, P. C., & Klein, K.-L. 1988, ApJ, 335, 940
Bontemps, S., André, P., Könyves, V., et al. 2010, A&A, 518, L85
Cambrésy, L. 1999, A&A, 345, 965
Chavarria-K, C., de Lara, E., Finkenzeller, U., Mendoza, E. E., & Ocegueda, J. 1988, A&A, 197, 151
Cohen, M., & Kuhi, L. V. 1979, ApJS, 41, 743
Condon, J. J. 1997, PASP, 109, 166
Dobashi, K., Uehara, H., Kandori, R., et al. 2005, PASJ, 57, S1
Duchêne, G., Bontemps, S., Bouvier, J., et al. 2007, A&A, 476, 229
Dunham, M. M., Allen, L. E., Evans, N. J., II, et al. 2015, ApJS, 220, 11
Dzib, S., Loinard, L., Mioduszewski, A. J., et al. 2010, ApJ, 718, 610
Dzib, S., Loinard, L., Mioduszewski, A. J., et al. 2011, RMxAC, 40, 231
Eiroa, C., & Casali, M. M. 1995, A&A, 303, 87
Eiroa, C., Djupvik, A. A., & Casali, M. M. 2008, in Handbook of Star Forming Regions, Vol. 2, The Southern Sky, ed. B. Reipurth (San Francisco, CA: ASP), 693
Eiroa, C., Torrelles, J. M., Curiel, S., & Djupvik, A. A. 2005, AJ, 130, 643
Erickson, K. L., Wilking, B. A., Meyer, M. R., et al. 2015, AJ, 149, 103
Evans, N. J., II, Allen, L. E., Blake, G. A., et al. 2003, PASP, 115, 965
Feigelson, E. D., & Getman, K. V. 2005, arXiv:astro-ph/0501207
Feigelson, E. D., & Montmerle, T. 1999, ARA&A, 37, 363
Giardino, G., Favata, F., Micela, G., Sciortino, S., & Winston, E. 2007, A&A, 463, 275
Greisen, E. W. 2003, in Information Handling in Astronomy: Historical Vistas, Vol. 285, ed. A. Heck (New York: Springer), 109
Gudehus, D. H. 2001, BAAS, 33, 850
Gutermuth, R. A., Bourke, T. L., Allen, L. E., et al. 2008, ApJL, 673, L151
Harvey, P., Merín, B., Huard, T. L., et al. 2007, ApJ, 663, 1149
Harvey, P. M., Chapman, N., Lai, S.-P., et al. 2006, ApJ, 644, 307
Heiderman, A., & Evans, N. J., II 2015, ApJ, 806, 231
Kaas, A. A., Olofsson, G., Bontemps, S., et al. 2004, A&A, 421, 623
Kern, N. S., Keown, J. A., Tobin, J. J., Mead, A., & Gutermuth, R. A. 2016, AJ, 151, 42
Kolesnik, I. G., & Iurevich, L. V. 1983, Afz, 19, 761
Könyves, V., André, P., Men'shchikov, A., et al. 2015, A&A, 584, A91
Kounkel, M., Hartmann, L., Loinard, L., et al. 2017, ApJ, 834, 142
Kuhn, M. A., Getman, K. V., Feigelson, E. D., et al. 2010, ApJ, 725, 2485
Mallick, K. K., Kumar, M. S. N., Ojha, D. K., et al. 2013, ApJ, 779, 113
Maury, A. J., André, P., Men'shchikov, A., Könyves, V., & Bontemps, S. 2011, A&A, 535, A77
Menten, K. M., Reid, M. J., Forbrich, J., & Brunthaler, A. 2007, A&A, 474, 515
Molinari, S., Brand, J., Cesaroni, R., & Palla, F. 1996, A&A, 308, 573
Ofek, E. O., & Frail, D. A. 2011, ApJ, 737, 45
Oliveira, I., Merín, B., Pontoppidan, K. M., et al. 2009, ApJ, 691, 672

Oliveira, I., Pontoppidan, K. M., Merín, B., et al. 2010, ApJ, 714, 778
Ortiz-León, G. N., Loinard, L., Kounkel, M., et al. 2017, ApJ, 834, 141
Ortiz-León, G. N., Loinard, L., Mioduszewski, A. J., et al. 2015, ApJ, 805, 9
Plunkett, A. L., Arce, H. G., Corder, S. A., et al. 2015, ApJ, 803, 22
Pontoppidan, K. M., van Dishoeck, E. F., & Dartois, E. 2004, A&A, 426, 925
Pradel, N., Charlot, P., & Lestrade, J.-F. 2006, A&A, 452, 1099
Preibisch, T. 1999, A&A, 345, 583
Rodríguez, L. F., Rodney, S. A., & Reipurth, B. 2010, AJ, 140, 968
Shuping, R. Y., Vacca, W. D., Kassis, M., & Yu, K. C. 2012, AJ, 144, 116
Smith, J., Bentley, A., Castelaz, M., et al. 1985, ApJ, 291, 571
Straižys, V., Černis, K., & Bartašiute, S. 1996, BaltA, 5, 125
Straižys, V., Černis, K., & Bartašiute, S. 2003, A&A, 405, 585
Thompson, A. R., Moran, J. M., & Swenson, G. W. 2007, Interferometry and Synthesis in Radio Astronomy (New York: Wiley)
Vallee, J. P. 1987, A&A, 178, 237
White, G. J., Casali, M. M., & Eiroa, C. 1995, A&A, 298, 594
Winston, E., Megeath, S. T., Wolk, S. J., et al. 2007, ApJ, 669, 493
Winston, E., Megeath, S. T., Wolk, S. J., et al. 2009, AJ, 137, 4777
Winston, E., Megeath, S. T., Wolk, S. J., et al. 2010, AJ, 140, 266
Xmm-Newton Survey Science Centre, C. 2013, yCat, 9044, 0
Zeilik, M., II, & Lada, C. J. 1978, ApJ, 222, 896
Zhang, C. Y., Laureijs, R. J., Wesselius, P. R., & Clark, F. O. 1988, A&A, 199, 170